Available online at www.sciencedirect.com
SCIENCE DIRECT®
Remote Sensing of Environment 103 (2006) 153–164
Remote Sensing of Environment
www.elsevier.com/locate/rse

Development of a daily long term record of NOAA-14 AVHRR land surface temperature over Africa

A.C.T. Pinheiro [a,*], R. Mahoney [b], J.L. Privette [a], C.J. Tucker [a]

[a] NASA GSFC, Greenbelt, MD, USA
[b] Global Science and Technology Inc., Greenbelt, MD, USA

Received 29 July 2005; received in revised form 15 March 2006; accepted 19 March 2006

Abstract

We developed a new 6-year daily, daytime and nighttime, NOAA-14 AVHRR based land surface temperature (LST) dataset over continental Africa for the period 1995 through 2000. The processing chain was developed within the Global Inventory Modeling and Mapping System (GIMMS) at NASA's Goddard Space Flight Center. This paper describes the processing methodology used to convert the Global Area Coverage Level-1b data into LST and collateral data layers, such as sun and view geometries, cloud mask, local time of observation, and latitude and longitude. We used the Ulivieri et al. [Ulivieri, C., M.M. Castronuovo, R. Francioni, and A. Cardillo (1994), A split window algorithm for estimating land surface temperature from satellites, *Adv. Space Research*, 14(3):59–65.] split window algorithm to determine LST values. This algorithm requires as input values of surface emissivity in AVHRR channels 4 and 5. Thus, we developed continental maps of emissivity using an ensemble approach that combines laboratory emissivity spectra, MODIS-derived maps of herbaceous and woody fractional cover, and the UNESCO FAO soil map. A preliminary evaluation of the resulting LST product over a savanna woodland in South Africa showed a bias of <0.3 K and an uncertainty of <1.3 K for daytime retrievals (<2.5 K for night). More extensive validation is required before statistically significant uncertainties can be determined. The LST production chain described here could be adapted for any wide field of view sensor (e.g., MODIS, VIIRS), and the LST product may be suitable for monitoring spatial and temporal temperature trends, or as input to many process models (e.g., hydrological, ecosystem).

Keywords: Land surface temperature; Advanced Very High Resolution Radiometer; Global Area Coverage; Split window algorithm; Africa

1. Introduction

Satellite land surface temperature (LST) products provide an estimate of the kinetic temperature of the earth's surface skin (Norman & Becker, 1995), i.e., the aggregate surface medium viewed by the sensor to a depth of about 12 μm. LST is a key parameter for the understanding of the physics of land surface processes (Sellers et al., 1988). It can be used for monitoring vegetation water stress, assessing surface energy balance, detecting land surface disturbance, and monitoring condition suitability for insect–vector disease proliferation, among other uses. Many of these applications are particularly important over the African continent given its large expanse and unique environmental conditions (e.g., strong wet/dry seasonality). Satellites offer the opportunity for the synoptic and continental or global monitoring of LST.

The National Oceanographic and Atmospheric Administration's (NOAA) Advanced Very High Resolution Radiometer (AVHRR) sensor has recorded top-of-atmosphere brightness temperature in two thermal infrared channels (TIR; channels 4 and 5) from 1981 to the present. These brightness temperatures depend on surface emittance, and atmospheric absorption and emission along the path of observation, among other factors. The surface emittance depends on the skin's kinetic temperature and emissivity.

At its coarsest resolution, AVHRR samples each 4 km (per side) at nadir, although pixel size increases with scan angle. Each Earth location is sampled at least once each day and once

* Corresponding author.
E-mail address: Ana.Pinheiro@gsfc.nasa.gov (A.C.T. Pinheiro).

0034-4257/$ - see front matter © 2006 Elsevier Inc. All rights reserved.
doi:10.1016/j.rse.2006.03.009

each night. Thus, the AVHRR record is valuable for monitoring and trending of many global change phenomena.

Several AVHRR-derived temperature products have been created to capitalize on the long term record of AVHRR thermal infrared measurements. For example, the second-generation of the Global Vegetation Index (GVI) dataset includes top-of-the-atmosphere brightness temperature values in channels 4 and 5 for the daytime overpasses of NOAA-9 and NOAA-11, from 1985 to 1994. The global products are provided at 0.15° resolution and at weekly and monthly time scales. An additional 5-year monthly climatology is also available (Gutman et al., 1995).

The World Land Surface Temperature Atlas dataset, produced by the European Space Agency, also provides an AVHRR temperature product. This dataset relies on brightness temperature data collected for years 1992 and 1993. The data consists of 1 km resolution LST fields over Europe, and a climatic monthly LST at half-degree resolution (Kerr et al., 1998). A more recent effort by Jin (2004) provides monthly diurnal-averages of 10-day composites of skin temperature fields from 1981 to 1998. The dataset is based on typical patterns of the LST diurnal cycle as determined with a General Circulation Model (GCM), and was scaled to 0.5° and 5° spatial resolutions.

Despite these efforts, no standard global daily AVHRR LST product exists (Wan et al., 2002). For more than two decades, the Global Inventory Modeling and Mapping System (GIMMS), at NASA's Goddard Space Flight Center, has produced global, multimission AVHRR vegetation index products. With its Global Area Processing System (GAPS; Tucker et al., 1994), GIMMS has significantly reduced product contamination from cloud, atmosphere, bidirectional reflectance and sensor artifacts. The scientific value of these products is evident in the major discoveries based on them (e.g., Myneni et al., 1997; Tucker et al., 2001; Nemani et al., 2003).

Although GIMMS has packaged AVHRR bands 4 and 5 with some products (e.g., the NASA AVHRR Pathfinder), it had no LST processing segment. In this article, we describe our adaptation of the GIMMS system to generate a standardized daily LST product over continental Africa. Our goal was to reuse validated GAPS segments (e.g., image navigation) to the extent possible, and develop new segments (e.g., emissivity mapping, LST estimation) as necessary. The resulting product spans a 6-year period (1995–2000), equivalent to the operational lifetime of the NOAA-14 satellite. It is designed to support multi-product long temporal studies as well as application and decision support systems (e.g., water resources management).

The outline of this article is as follows. First, we describe characteristics of the AVHRR and NOAA orbiters. We then present the methodology and algorithms developed to generate the new LST product, including the processing system used to convert the Level-1b Global Area Coverage (GAC) data into top-of-atmosphere brightness temperature. We particularly emphasize the preproduction estimation of surface emissivity in the AVHRR bands, since no prior maps existed to our knowledge. Collateral data fields, such as cloud mask and the local solar time of observation, are also described. We conclude with an evaluation of the LST product over a savanna woodland in southern Africa.

2. Data

2.1. NOAA-14 AVHRR

Our LST product is derived from the AVHRR sensor onboard NOAA-14, a polar-orbiting satellite in NOAA's Polar Operational Environmental Satellites (POES) constellation. Below we briefly describe aspects of POES and AVHRR relevant to this article. Readers desiring further details are encouraged to consult Kidwell (1991) or Cracknell (1997).

The POES satellite orbits are nominally sun synchronous. They have an orbital inclination of 98.9° and period of approximately 102 min, resulting in 14.1 orbits per day. Consecutive equatorial crossings are separated by about 25.5° longitude (at the equator), moving from East to West with time. The orbital characteristics allow the sensor to view an earth location under the same geometric conditions (sun and view angles) each 9 days. Under nominal conditions, NOAA-14 crosses the equator in ascending node (from South to North) at a local crossing time of 13:30 (Kidwell, 1991). However, the orbit 'drifted' to later crossing times (up to 16:30) through its operational lifetime (Price, 1991).

The Advanced Very High Resolution Radiometer Version 2 sensor (AVHRR/2) on NOAA-14 is a cross-track scanning system with five spectral channels (Table 1). Each channel has a nominal spatial resolution of 1.1 km at nadir. The AVHRR/2 rotating mirror measures radiances to approximately ±55° off nadir, which corresponds to approximately a ±68° view zenith angle for pixels at the edge of scan. The ground swath is about 2800 km wide.

The commonly-used AVHRR Global Area Coverage (GAC) product, which offers complete global coverage at reduced spatial resolution, is created onboard the sensor in real time. A GAC pixel value represents the mean of four out of each five consecutive samples along the scan line; only data from each third scan line are processed and stored. As a result, the spatial resolution of GAC data near nadir is about 1.1 by 4 km with a 3 km gap between pixels across the scan line. Many users approximate a GAC pixel as 4.4 km resolution (Fig. 1).

Table 1
Channel characteristics of the NOAA-14 AVHRR/2

Channel	Spectral domain	Spectral range (FWHM#)	IFOV*(mrad × mrad)
1	Visible	0.58–0.68	1.31 × 1.33
2	Near infrared	0.73–1.10	1.31 × 1.29
3	Middle infrared	3.55–3.93	1.20 × 1.30
4	Thermal infrared	10.3–11.3	1.27 × 1.49
5	Thermal infared	11.5–12.5	1.13 × 1.27

FWHM = Full Width Half Maximum of the spectral response function.
* IFOV = Instantaneous Field of View; The AVHRR has a square shaped detector so the IFOV for each channel has two values. In each dimension, the IFOV resembles a Gaussian distribution, and the nominal IFOV is the FWHM value (ITT, 1994).

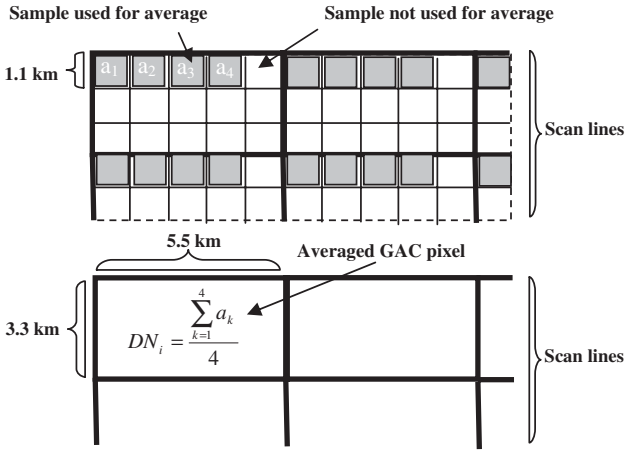

Fig. 1. Sampling scheme for AVHRR GAC data.

We estimate LST using the two longwave thermal infrared bands (channels 4 and 5). These bands were primarily designed to detect clouds and measure sea surface temperature, however they have increasingly been exploited for other applications (e.g., to detect wildfires). Their land utility is limited, however, since the saturation temperature in channel 4 is 323 K. This temperature is commonly exceeded by top-of-atmosphere (TOA) brightness temperatures over arid lands, which both limits LST accuracy (Pinheiro et al., 2004) and fire detection potential (Giglio & Justice, 2003).

3. Methods

We provide brief details on each major segment of our LST processing system, starting with previously-developed segments (e.g., from GAPS or in published literature), then moving to newly-developed segments (e.g., emissivity fields). A schematic representation (Fig. 2) of the chain serves as a roadmap to this section.

3.1. General processing segments

3.1.1. Data ingest, calibration and navigation

Our system ingests NOAA-14 AVHRR/2 GAC data in Level-1b format. We obtain these as global granules from NOAA Satellite Active Archive (http://www.saa.noaa.gov; now called the Comprehensive Large Array data Stewardship System, or CLASS). We subset these for the African continent and distinguish between daytime and nighttime overpasses. We extract the GAC image data (digital numbers for the 5 different channels) as well as the metadata, including the time code (year, Julian day, and UTC time of day in milliseconds), quality control (QC) indicators, calibration coefficients (slope and intercept values for each of the five channels), zenith angles and Earth location.

The calibration of the AVHRR/2 thermal infrared channels is accomplished in two steps using a linear radiometric calibration and a subsequent non-linear radiometric calibration. The sensor was designed to view cold space and internal warm blackbodies as part of its normal scan sequence. This provides data for determining signal-to-noise ratio, radiometric slopes (gains) and intercepts (offsets). The gains and offsets are applied to the sensor counts of the ground target (digital counts) to estimate an assumed "linear" radiance, following Eq. (1):

$$L_i = S_i X + I_i \tag{1}$$

where L_i is the radiance in mW/(m^2 sr cm^{-1}), X is the input digital number (ranging from 0 to 1023 counts), and S_i and I_i are respectively the scaled slope and intercept values. The scaled thermal channel slope values are in units of mW/(m^2 sr cm^{-1}) per count, and the intercept is in mW/(m^2 sr cm^{-1}). Because channels 4 and 5 use HgCdTe detectors, their calibration are slightly non-linear. Beginning with NOAA-13 AVHRR instrument, a new non-linear radiometric calibration of those two channels is adopted following Eq. (2):

$$L_i' = AL_i + BL_i^2 + C \tag{2}$$

where L_i' is the corrected radiance, and A, B and C are coefficients (see Table 2), specific to each sensor. For more details on AVHRR thermal infrared channels calibration consult Kidwell (1995).

We convert radiances into top-of-atmosphere brightness temperatures using the sensor spectral response function

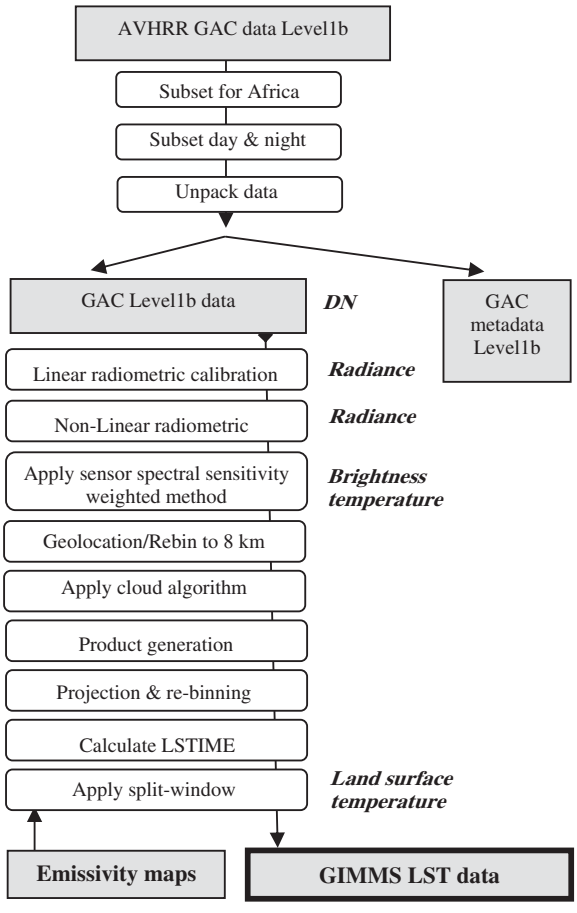

Fig. 2. Schematic representation of NOAA-14 AVHRR GIMMS LST data set processing system for the thermal infrared channels.

Table 2
Non-linear radiometric calibration for NOAA-14 AVHRR/2 channels 4 and 5

Coefficient	Channel 4	Channel 5
A	0.92378	0.96194
B	0.0003822	0.0001742
C	3.72	2.00

weighting method and the Planck function, i.e., assuming that Earth emits as a blackbody in the spectral wavelength of interest, such that,

$$T(R) = \frac{c_2 v}{\ln\left(1 + \frac{c_1 v^3}{L}\right)}, \quad (3)$$

where T is the temperature in Kelvins for the radiance value L, v is the wave number of interest (in cm^{-1}), and c_1 (1.1910659×10^{-5} mW m^{-2} sr^{-1} cm^4) and c_2 (1.438833 cm K) are the Planck constants. Since the above equation is not easily inverted, we constructed a look-up table of brightness temperature–radiance pairs for each channel, at increments of 0.01 K. We assume the valid range of brightness temperatures is between $230\ \mathrm{K} \le T(L) \le Tb$(saturation), where Tb(saturation) corresponds to the upper limit of the given channel's dynamic range (Table 3). In cases where either channel saturates in our data set (e.g., over African deserts during the summer; Prata, 2000), we replace the estimated LST with a fill value of −999.

3.1.2. Cloud mask

We implemented *CL*ouds for *AVHR*R-Phase 1 (CLAVR-1), a day and night global cloud detection algorithm developed for AVHRR GAC data (Stowe et al., 1999). The CLAVR-1 algorithm was designed for operational real time processing, and it classifies each 2×2 GAC pixel array (adjacent pixels on adjacent scan lines) as clear or other condition. The algorithm is composed of four different algorithms, each appropriate for one of the following sampling cases:

(i) over land, for day time overpasses;
(ii) over land, for nighttime overpasses;
(iii) over ocean, for day time overpasses;
(iv) over ocean, for nighttime overpasses.

CLAVR-1 uses the five AVHRR channels and exploits their differing sensitivities to different atmospheric conditions. The approach is based on a multispectral, sequential, decision-tree algorithm, where three different tests are applied: a) *contrast signature tests*, b) *spectral signature tests*, and c) *spatial signature tests*. The resulting cloud mask follows the classification scheme defined in Table 4. Interested readers may consult Stowe et al. (1999) for further details.

Following the identification of cloudy and clear pixels, we create a set of products, scale them and write the data into binary files. The resulting products are shown in Table 5.

Table 3
Brightness temperature, *Tb*(saturation), at upper limit of dynamic range of AVHRR thermal channels (Cracknell, 1997)

Channel	*Tb* (saturation)
3	~ 322 K
4	~ 323 K
5	~ 330 K

Table 4
CLAVR cloud mask classification

Land		Ocean	
Condition	Flag	Condition	Flag
Clear	3	Clear	1
Dark Dense Vegetation (DDV)	4	Glint	2
Cloudy or mixed	6	Cloudy or mixed	5
Shadow	8	Shadow	7

3.1.3. Image geolocation and projection

We geolocate the AVHRR scenes following Rosborough et al. (1994), adapted to ingest NORAD ephemeris data (Celestrak; http://www.celestrak.com). We remapped and re-binned the data into Albers Equal Area projection with an 8 by 8 km grid cell size such that it is compatible with the GIMMS Normalized Difference Vegetation Index (NDVI) data set (Tucker et al., 1994). Where multiple AVHRR pixels are projected into a single grid cell, we select and store the pixel with the maximum brightness temperature in channel 5 (T_5). We assume that this sample is least likely to have sub-pixel cloud contamination.

For each grid cell value, we compute the local solar time (LSTIME) of observation by adjusting the equatorial crossing time (TIME) files for longitudinal variation for each observation, according to Eq. (3).

$$\mathrm{LSTIME} = \mathrm{TIME} + \frac{\mathrm{LON}}{15}. \quad (3)$$

3.2. Estimating LST From AVHRR

To retrieve LST from the AVHRR top-of-atmosphere brightness temperature measurements, we chose a "split window" algorithm. This approach, based on an empirical inverse model, is derived from a first order expansion of the Taylor series applied to the Planck function. It takes advantage of the differential atmospheric absorption in two spectrally close thermal infrared bands to (largely) compensate for the effects of

Table 5
Products generated for each cloud-free pixel

Products *	Scaling factor
T4 — Brightness temperature for channel 4	10
T5 s — Brightness temperature for channel 5	10
TV s — View zenith angle	100
TS s — Solar azimuth angle	100
FV s — View azimuth angle	100
FS — Solar azimuth angle	100
LAT — Latitude	100
LON — Longitude	100
TIME — Time of latitudinal crossing	100

* All fields are stored as 2-byte integers.

absorbing gases. In the case of the AVHRR sensors, channels 4 and 5 are used. The algorithm assumes that atmospheric attenuation (due mostly to atmospheric water vapor) is greater in channel 5 than in channel 4, and that the difference in measured radiance between the two channels increases with increasing water vapor.

For AVHRR, the relationship between LST and measured brightness temperature in the two channels (T_4 and T_5) can be formulated as follows:

$$\mathrm{LST} = T_4 + a_1(T_4 - T_5) + a_0, \tag{4}$$

where coefficient a_1 is a constant dependent upon atmospheric type (e.g. polar, temperate, and tropical) and accounts for water vapor absorption and atmospheric emission. The relationship above also accounts, in a static or dynamic way, for the surface behaving as a selective radiator, i.e. with variable emissivity. In practice, both a_0 and a_1 are determined by applying a regression to modeled relationships found between the channels' brightness temperatures for different atmospheric and surface scenarios.

3.2.1. Ulivieri's split window LST algorithm

We adopted the split window algorithm developed by Ulivieri et al. (1994) due to its simplicity, robustness and superior performance in independent tests (Becker & Li, 1995; Vazquez et al., 1997; Yu et al., submitted for publication). Ulivieri's algorithm can be written as,

$$\mathrm{LST} = T_4 + 1.8(T_4 - T_5) + 48(1-\varepsilon) - 75\Delta\varepsilon, \tag{5}$$

where T_4 and T_5 are the top-of-atmosphere brightness temperatures of AVHRR channels 4 and 5, respectively and,

$$\Delta\varepsilon = \varepsilon_4 - \varepsilon_5 \tag{6}$$

$$\varepsilon = \frac{\varepsilon_4 + \varepsilon_5}{2} \tag{7}$$

Eq. (5) was developed for cases of column atmospheric water vapor less than 3.0 g/cm^2, a reasonable condition for much of the semi-arid portions of continental Africa. Becker and Li (1995) tested the Ulivieri algorithm using four different data sets as part of an intercomparison between seven different LST split window algorithms. In all cases, the Ulvieri algorithm performed well. A later algorithm comparison (Vazquez et al., 1997) yielded similar results, and indicated that the Ulivieri algorithm was least dependent on accurate knowledge of surface emissivity of the algorithms tested. Yu et al. (submitted for publication) tested the sensitivity of 10 different split window algorithms to uncertainties in surface emissivity, view zenith angle, and surface-air temperature differences. They found Eq. (5) was among the two most stable algorithms.

3.3. Surface emissivity

In the Ulivieri algorithm, surface emittance is represented by two terms; the first depends upon the average behavior of the surface as a selective radiator (ε), the second upon its spectral emittance ($\Delta\varepsilon$). This presents a challenge for an operational algorithm since there are few global data sets of spectral emissivity. To our knowledge, none exist at 8 km resolution (or finer) and for AVHRR channels 4 and 5 at the time this work was developed.

3.3.1. Development of a moderate resolution emissivity maps

Pixel emissivity is difficult to retrieve remotely since a brightness temperature measurement represents the convolution of surface emissivity and the emittance of a blackbody of unknown kinetic temperature. Thus, in the inverse problem, the number of unknown variables (emissivity and kinetic temperature) exceeds the number of known data values (measured brightness temperature). Some methods have been proposed to estimate emissivity from AVHRR observations (Becker & Li, 1990; Van de Griend & Owe, 1993; Becker & Li, 1995; Sobrino et al., 2001), but these have not been validated over large scales (e.g., continents). More sophisticated methods (e.g., Becker & Li, 1990) are computationally expensive, and require accurate knowledge of the atmospheric profile as well as the existence of non-cloudy conditions for a day and night observation pair.

To facilitate the use of Ulivieri's algorithm over Africa, we developed an emissivity map by combining state-of-the-art land cover maps with laboratory emissivity spectra. Specifically, we assume that an AVHRR pixel's emissivity can be estimated as the spatially-weighted ensemble of its endmember emissivities, i.e.,

$$\langle \varepsilon_i \rangle = \sum_{k=1}^{N} \varepsilon_{k_i} f_k \tag{8}$$

The pixel ensemble emissivity, $\langle \varepsilon_i \rangle$, where i denotes the thermal channel, is a function of the endmember channel emissivities, ε_{k_i}, and the fractional cover of the endmembers, f_k. We define an "endmember" as a class of scene components assumed to have the same emissivity, such as tree crown, herbaceous background, or bare soil background. We determined the endmember types and fractions using soil and vegetation maps, and we determined the endmember emissivities using spectral libraries.

We prescribed the spatial distribution of soil types using the FAO Soil Map of Africa (FAO–UNESCO, 1987). For each type, we estimated the AVHRR band emissivity (Table 6) by convolving the associated emissivity spectra (available from Jet Propulsion Laboratory (JPL), www.jpl.nasa.gov) with the relative spectral response functions for AVHRR/2 channels 4 and 5. Direct association between the FAO soil types and the JPL spectra was not always possible since the thematic classification of the spectra is based on the US soil classification system, whereas FAO uses its own system. In unclear cases, we associated the soil property descriptions between the two systems. Where multiple JPL spectra were available for a given soil class, we averaged the spectra before applying the AVHRR spectral sensitivity functions.

Extending the static landcover approach of Wilber et al. (1999), we created two layers of vegetation emissivity for each pixel: one layer for woody (tree) vegetation and one for

Table 6
Average emissivities for AVHRR channels 4 and 5 assigned to each soil class

Soil class	Emissivity	
	Channel 4	Channel 5
Mollisols	0.973	0.978
Vertisols	0.973	0.980
Ultisols	0.961	0.975
Inceptisols	0.970	0.974
Alfisols	0.969	0.976
Entisols	0.973	0.980
Solonchaks	0.975	0.975
Aridisols	0.969	0.974
Oxisols	0.977	0.976
Spodosols	0.970	0.971
Histosols	0.973	0.978
Rockland	0.954/0.977	0.940/0.968
Rock	0.954	0.940
Salt	0.975	0.975
Water	0.994	0.986

Note 1: No data available for Oxisoils class. We adopted the emissivity for Alfisols class which has similar physical description in the epipedon (surface layer) — "reddish brown fine sandy loam".
Note 2: Default rockland is granite in all areas, with exception of soils in Kenya where rockland is assumed to be basalt.

herbaceous vegetation. To determine the fractional cover of each layer, we used the continuous field data from Hansen et al. (2000). We determined the AVHRR emissivity values (Table 7) according to the convolution approach described above for soils. We associated the JPL *conifer* spectra with UMD evergreen forest class, the *deciduous* spectra with the deciduous forest class and the *grass* spectra with the grassland and agricultural classes. The reflectance spectra for each of these are shown in Fig. 3. Emissivity spectra were determined by subtracting spectral reflectance from unity.

Following Eq. (8), we calculated the ensemble emissivity for each pixel by weighting the endmember emissivities by their cover fraction as specified in the UMD continuous field product for woody cover, bare soil cover and herbaceous cover. By combining the continuous fields product with a static land cover data set, we created a fixed emissivity map that responds to both inter- and intra-class variability. We used this map for all processed scenes. The results for channel 4 and 5 are shown in Fig. 4a and b, respectively.

Table 7
Average emissivities for AVHRR channels 4 and 5 assigned to each vegetation class

Land cover type (UMD land cover class)	Emissivity	
	Channel 4	Channel 5
Evergreen forest (1, 2)	0.989	0.991
Deciduous forest (3, 4)	0.974	0.973
Mixed forest (5)	0.982*	0.982*
Woodland (6)	0.982*	0.982*
Wooded grassland (7)	0.982*	0.982*
Closed shrubland (8)	0.982*	0.982*
Open shrubland (9)	0.982*	0.982*
Grassland (10)	0.982	0.989
Agricultural (11)	0.982	0.989

Note*: average of 50% evergreen and 50% deciduous.

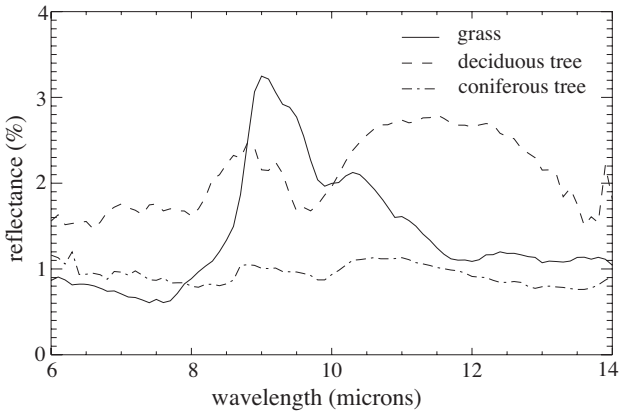

Fig. 3. Spectral reflectance for grass, conifer tree and deciduous tree. Source: JPL spectral library.

3.4. Generation of the continental AVHRR data set

We systematically processed 6 years of daily (day and night) AVHRR/2 GAC data at 8 km resolution using the processing chain outlined in Fig. 2. The resulting data set consists of a set of flat binary data files for each day or night. The science data sets are stored as two-byte integers, and include the LST, the channel 3, 4 and 5 top-of-atmosphere brightness temperatures, the local solar time of observation, the cloud mask, and the sun and view geometries (zenith and azimuth angles). Reference latitude, longitude and emissivity maps and a land–water mask accompany these data sets. The 6-year data set is archived at the Oak Ridge National Lab (ORNL) Distributed Active Archive Center (DAAC).

4. Product evaluation

Given the lack of suitable independent LST data sets over Africa, we focused our product evaluation effort on the effectiveness of the split window algorithm in correcting for water vapor attenuation rather than determining the LST uncertainty across the continent. To do so, we compared the AVHRR/2 LST product to LST field measurements collected over a savanna near Skukuza, South Africa (inside Kruger National Park) between March and November of Year 2000. The evaluation is limited to Year 2000 dates given the unavailability of field data earlier in the NOAA-14 lifetime. The Skukuza site features a mixture of *combretum* and *acacia* species sparsely distributed over a grassy background (see Table 8 for surface characteristics, or Scholes et al., 2001 for a general site description). The vegetation is subjected to extensive browsing and grazing through the year, and wildfires typically consume the grasses (but not tree crowns) once during the dry season (June–September).

4.1. Approach

Given the three-dimensional vegetation structure of the site, we estimated the fraction of each scene endmember visible to the AVHRR using the Modified Geometrical Projection (MGP;

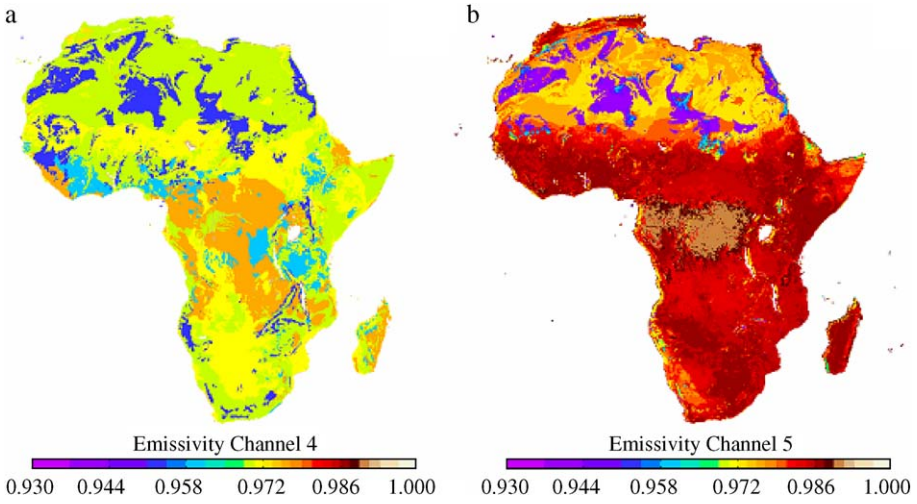

Fig. 4. a) Ensemble emissivity maps for AVHRR channel 4 b) and channel 5.

Pinheiro et al., 2006) model and the sun-view geometry of the AVHRR observation. The model configuration assumed that the savanna was composed of just two endmembers (tree crown and background). Following Pinheiro et al. (2004), we then used a weighted ensemble method to estimate the pixel-scale radiometric temperatures detectable to AVHRR from the field-measured endmember temperatures.

To assign endmember temperatures, we used field data from two precision infrared thermocouple transducers (Model IRTS-P; Apogee Instruments Inc., Logan, Utah), hereafter referred to as Apogee-TIR sensors, mounted on vertical poles. Each sensor was aimed at a relatively homogeneous endmember, including a tree crown (sensor mounted 7 m above target) and a grassy background (sensor mounted 2 m above target), respectively. The Apogee TIR sensors collected samples each 10 min, and we recorded the average of these samples each 30 min. The manufacturer claims that the accuracy of the IRTS-P is 0.4 °C from 5 to 45 °C and 0.2 °C from 15 to 35 °C. Independent analysis confirmed that the measured targets were acceptable representatives of the populations of endmembers in the area (Pinheiro et al., 2006). Further details on field site, sensor configuration, Apogee data processing and results are available in Pinheiro et al. (2006).

The Apogee-TIR data represent the sum of reflected irradiance and endmember emittance over the target. After converting the Apogee TIR temperature data (K) to flux (W/m^2) using the Stefan–Boltzmann equation, we determine the endmember emittance by subtracting the reflected irradiance. To estimate the ensemble emittance $\langle M_{\text{ensemble}}\rangle$ [W/m^2], we weighted each endmember emittance with the respective fractional cover and summed the results, i.e.,

$$\langle M_{\text{ensemble}}\rangle = f_{\text{crown}}(\sigma Tb^4_{\text{crown}} - (1-\varepsilon_{\text{crown}})E_{\text{atmos}}\downarrow) + f_{\text{background}}(\sigma Tb^4_{\text{background}} - (1-\varepsilon_{\text{background}})E_{\text{atmos}}\downarrow) \quad (9)$$

where the Tb_{crown} and $Tb_{\text{background}}$ are radiometric temperatures measured by Apogee TIR sensors for crown and background, respectively, and σ is the Stefan–Boltzmann constant (5.67×10^{-8} W m^{-2} K^{-4}). We calculated the emissivities for crown and background, $\varepsilon_{\text{crown}}$ and $\varepsilon_{\text{background}}$, by assuming a uniform spectral response for the Apogee TIR sensor over its spectral sensitivity range (6 to 14 μm), and using spectral reflectance data from the ASTER Spectral Library (http://speclib.jpl.nasa.gov) and assuming complementarity between emissivity and reflectance (i.e., Kirchoff's Law). The sky irradiance, $E_{\text{atmos}}\downarrow$ [W/m^2], was measured by a pyrgeometer (Model CG1, Kipp and Zonen, Delft, Holland) mounted on a nearby tall tower. The pyrgeometer measured infrared (5 to 45 μm) radiant flux to an accuracy specified of +10%. Although the Apogee-TIR sensors and pyrgeometer were sensitive to different spectral windows, no data adjustment was attempted.

To estimate the ensemble LST, we divided the ensemble emittance by the ensemble emissivity and the Stefan–Boltzmann constant, and took the fourth root, i.e.,

$$\langle T_{\text{ensemble}}\rangle = \sqrt[4]{\frac{\langle M_{\text{ensemble}}\rangle}{\sigma\langle\varepsilon\rangle}} \quad (10)$$

where the ensemble emissivity, $\langle\varepsilon\rangle$, is estimated as

$$\langle\varepsilon\rangle = \varepsilon_{\text{crown}} f_{\text{crown}} + \varepsilon_{\text{background}} f_{\text{background}}. \quad (11)$$

Table 8
Skukuza vegetation structural characteristics

Parameter	Quantity
Maximum height of crown center	8.20 m *
Minimum height of crown center	2.07 m #
Average canopy horizontal radius	2.65 m
Average canopy vertical radius	3 m
Woody cover (tree+shrub)	31%
Tree density	127 ha^{-1}
Maximum tree LAI (February)	0.67
Minimum tree LAI (June)	0.15

* 2/3 of maximum tree height.
\# 2/3 of minimum tree height.

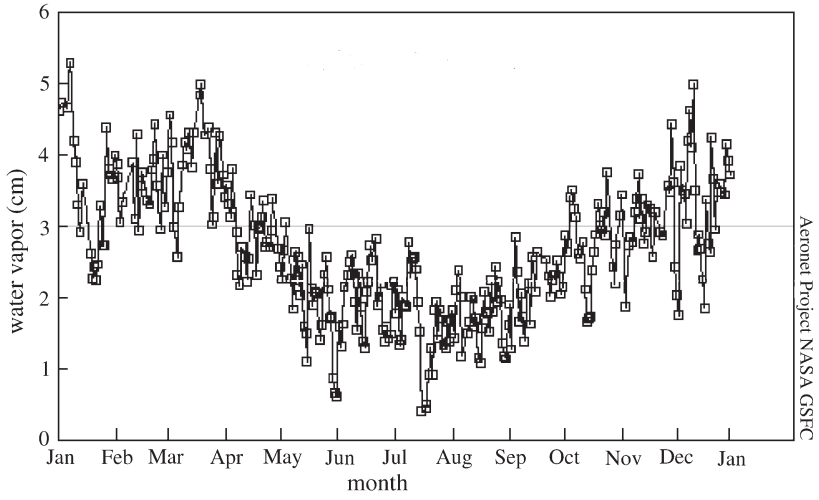

Fig. 5. Seasonal cycle of water vapor content for the year 2000 retrieved by the AERONET at the Skukuza site. It is clear that the Ulivieri split window algorithm threshold of 3 cm is violated from about October to May. Modified from http://aeronet.gsfc.nasa.gov/.

Clearly, these statistically-based estimations (including mean wide-band emissivities) are not as rigorous as line-by-line calculations, however we believe the cumulative uncertainty is commensurate with the other uncertainties (e.g., spatial scale differences) in this comparison.

5. Results

We compared $\langle T_{\text{ensemble}} \rangle$ from Eq. (10) with the pixel value from our AVHRR/2 LST product for a series of days in Year 2000. The AVHRR LST had a relatively low overall bias, in all cases below 0.3 K. The uncertainty, defined here as the root mean square error (RMSE), for the entire period was 1.24 K for daytime observations and 2.38 K for nighttime observations.

As noted above, the Ulivieri split window algorithm was developed for atmospheric conditions with column water vapor less than 3 g cm^{-2}. AERONET sunphotometer (Holben et al., 1998) data in year 2000 indicate that this condition was often violated at Skukuza. Violations particularly occurred during the wet season (~ October through April) as shown in Fig. 5. Therefore, we independently evaluated the AVHRR/2 LST product performance under dry season conditions (i.e., ~ June through August; Fig. 6). In this case, the RMSE was 0.92 and 2.46 K for the day and night, respectively (see Table 9).

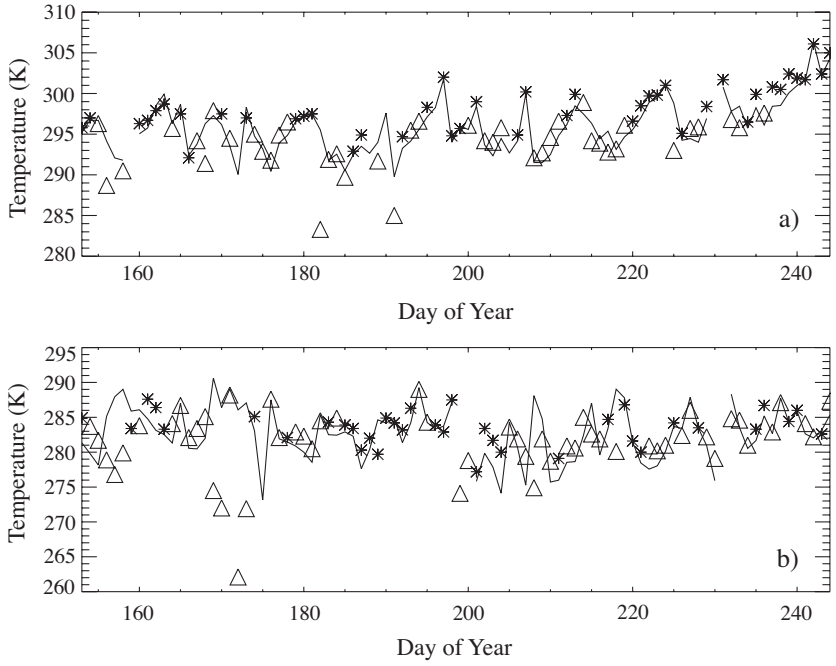

Fig. 6. Comparison of field derived ensemble surface temperature (–) and AVHRR LST at the Skukuza site for day (a) and night (b). Clear (*) and cloudy or shadowed conditions (Δ) AVHRR retrievals are distinguished.

Table 9
Error statistics determined through comparisons of AVHRR LST and field-measurements

	Bias (mean)	Precision (SD)	Uncertainty (RMSE)
All samples			
Daytime (N=94*)	0.15	0.79	1.24 K
Nighttime (N=97*)	0.29	1.53	2.38 K
Dry season subset (June 1st–August 31st 2000)			
Daytime (N=45*)	0.08	0.40	0.92 K
Nighttime (N=38*)	0.17	1.00	2.46 K

*N = number of clear sky data points used to determine the statistical values.

The improvement in product performance is clear, although the uncertainty (RMSE) during nighttime condition inexplicably increased slightly.

6. Discussion

Our validation results are encouraging, however they are quite limited and must be viewed with significant caution given the mismatch in scale between the endmember temperature measurements (10^0 m^2) and the AVHRR/2 LST grid cell (10^7 m^2). Further, the LST uncertainties must be considered in light of typical LST applications. For example, a 0.5 K LST error can lead to a 10% error in sensible heat flux (Brutsaert et al., 1993), a 1 K error can result in a 10% error in evapotranspiration (Moran & Jackson, 1991), and 1–3 K errors can lead to surface flux errors of up to 100 W/m^2 (Kustas & Norman, 1996). In this sense, our products are best used for relative assessments, such as comparisons in space or time, rather than for absolute values. This is probably true for any satellite-derived LST product at present. Below we describe the key error sources in our methodology.

Inspection of the area using aerial photography and Landsat imagery suggests that the Skukuza field site area (at the scale of the AVHRR pixel) is heterogeneous. Natural variability within a given endmember class (e.g., tree crown) creates uncertainty in the representativeness of the point sampling. Pinheiro et al. (2006) showed that the Apogee values were within about one standard deviation of the mean for the endmember population, however that evaluation only considered endmembers at equally-spaced points within a limited grid (10^5 m^2) and for limited time periods.

Further, our field-derived temperature estimation ignores the vertical profile of the vegetations' temperature and does not differentiate between sunlit and shaded surfaces. Still, temporal temperature profiles suggest the latter effect is less significant at the drifted AVHHR overpass times (around 16:00 in Year 2000) compared to immediate postlaunch overpass times (Pinheiro et al., 2004). A more comprehensive field data set would likely provide much better insight into performance of the AVHRR LST product and potentially allow us to prioritize the error sources noted below.

As shown in Table 9, our AVHRR LST is more accurate in the dry (winter) season when the atmosphere is colder and contains less water vapor. In general, the precision of any split window LST algorithm degrades in warmer temperatures (290–305 K) and with larger view zenith angles. Both conditions tend to result in greater gaseous absorption along the observation path, and increasingly second-order atmospheric effects not captured in simple split window formulations result in performance degradation.

The poorer nighttime results, versus those in the daytime, were not expected because more uniform radiative cooling processes dominate and the range of endmember temperatures is more limited at night. Our results may have been caused by poor detection of (sub-pixel) clouds at night, since CLAVR accuracy degrades at night in mid-latitudes (Stowe et al., 1999).

Recent work (Yu et al., submitted for publication) demonstrates the high sensitivity of split window LST algorithms to surface emissivity accuracy. Although we developed an emissivity database in the present work that partly accounts for variable canopy types and fractional covers and different soil types, it represents only a rough estimation. It relies on a remotely-sensed UMD continuous fields product of unknown accuracy, and on laboratory emissivity data that likely differ significantly from aggregate canopy values. Further, the extent of the laboratory spectral library is obviously limited. All of these data sets are static and therefore we do not account for local phenological and environmental changes in time. To our knowledge, recent efforts to develop continental scale emissivity maps based on the MODIS emissivity product remain unvalidated to date. However, advances by both the MODIS and ASTER teams suggest that accurate and dynamic emissivity maps may be possible in the coming years.

Finally, there are limitations with the AVHRR sensor itself. The absolute radiometric accuracy of AVHRR is approximately 0.55 K (Weinreb et al., 1990). Further, AVHRR band-to-band collocation errors (approximately 0.1 mrad) can produce errors in LST of about ±0.1 K for a structured scene with a mean temperature of 300 K and inter-pixel spatial variability of 10 K (Prata, 1994). In the same study, Prata (1994) reports that georegistration errors may average ±0.5 K for day time observations and ±0.2 K for nighttime observations. Readers should consult Prata (1994) for a detailed analysis.

Clearly, validation of any continental-scale LST product is challenging since LST can vary significantly within a pixel area and change within relatively short time periods. Moreover, the number of in situ observations that match satellite observations in both time and space is limited. Unfortunately, the validated LST products from the Earth Observing System (EOS; e.g., Wan et al., 2002) overlapped the NOAA-14 operational lifetime only in year 2000. By that point, the NOAA-14 equator crossing time had drifted to late afternoon (after 1600 h). Thus, LST products from EOS Terra (equator crossing at 1030 h) could not be credibly used. Further validation work, conducted under many different conditions (e.g., at the scale of EOS validation; Morisette et al., 2002), is needed before we can confidently assign uncertainties to this data set.

It is important to remind readers to use caution in any use of an AVHRR-derived LST or SST data set. As noted above, equator crossing times of NOAA afternoon satellites drift substantially with time past launch. Although the nominal,

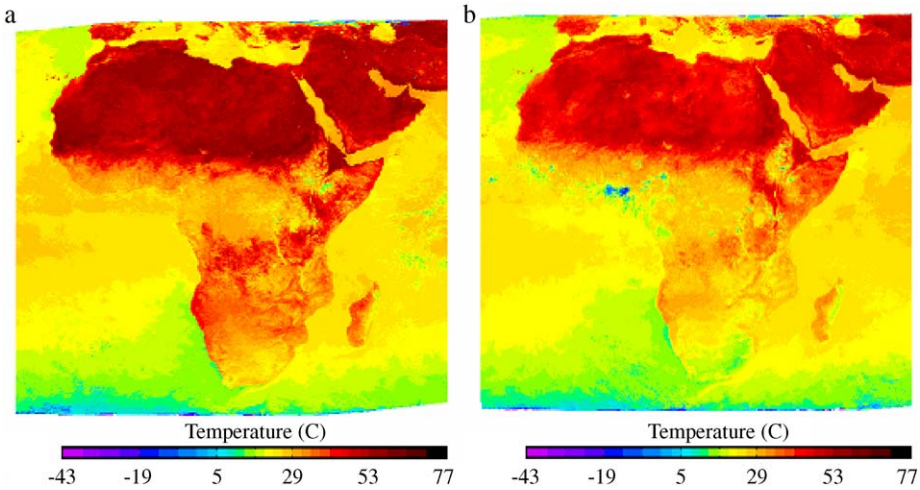

Fig. 7. Composite AVHRR-derived land surface temperature for a) July 1996 (overpass around 1:30 PM) and b) July 2000 (overpass around 4:00 PM). The compositing process (maximum temperature over the month was retained) removed most of the clouds. However, some clouds are visible (blue areas) near the equator in b). We did not use information available in our product's auxiliary cloudiness field for this demonstration. (For interpretation of the references to colour in this figure legend, the reader is referred to the web version of this article.)

immediate post-launch crossing time for NOAA-14 was 1330 PM, the orbit degraded at a rate of approximately 1/2 h per year thereafter (Price, 1991; Privette et al., 1995). As the orbit decays, the LST values trend to lower values as shown in Fig. 7. The apparent cooling is due to mechanical causes (the drift in AVHRR overpass time) rather than natural causes. Several correction approaches have been published (Gutman, 1999; Jin and Treadon (2003), although each requires significant assumptions which tend to be violated on a per-pixel scale.

A second AVHRR temporal sampling issue is more insidious. Since AVHRR scans the earth's surface with angles of ±55° from nadir (equivalent to ±68° on the surface), an AVHRR swath crosses more that 2.5 time zones (i.e., 2.5 h local time) at the equator. Thus, pixels on opposites edges of a single AVHRR scan may be sampled at significantly different local solar times. The consequent differences in solar zenith angles and heating periods (thermal inertia effects) can lead to systematic temperature differences.

Lastly, given the AVHRR wide field of view and NOAA orbit periodicity of 9-days, AVHRR effectively observes the same earth target under the same geometric (observation and illumination) conditions once each 9 days. Pinheiro et al. (2004) recently showed that variation in observation and illumination geometry of AVHRR sampling leads to measurable artifacts in LST estimates in the presence of structured vegetation. These angular effects, identified in previous studies (e.g., Caselles & Sobrino, 1989), can lead to systematic LST biases, including 'hot spot' effects when no shadows are observed. In the case of a woodland area, 'hot-spot' values (where the solar and view vectors coincide and therefore no shadows are visible) were up to 9 K higher than those at non-hot spot geometries. Fig. 8 illustrates an example of the angular dependency of AVHRR LST retrievals over sparse vegetations, in this case in Ghanzi, Botswana, a shrubland surface in southern Africa. The daily daytime values of AVHRR LST depict a similar pattern to the distribution of view zenith angles over time.

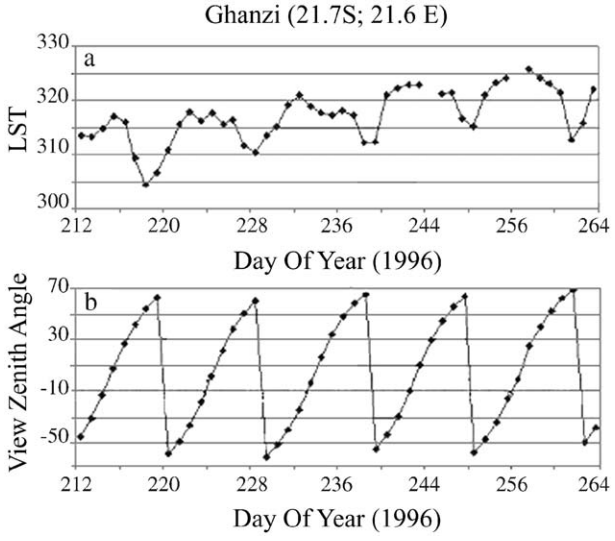

Fig. 8. Daily daytime AVHRR a) Land Surface Temperature (LST) and b) view zenith angle for Ghanzi, Botswana.

7. Conclusions

We have developed a new daily, daytime and nighttime, AVHRR/2 Land Surface Temperature (LST) product based on Global Area Coverage (GAC) data over continental Africa. The production system borrows many validated segments from NASA's GIMMS system, which is used to produce high level AVHRR vegetation index products. We augmented this system with published cloud clearing (CLAVR-1) and LST split window (Ulivieri et al., 1994) algorithms. In addition, we developed new emissivity maps of Africa for AVHRR channels 4 and 5 by combining laboratory field spectra with estimates of

each grid cell's fraction of exposed soil, understory and overstory vegetation. The resulting processing chain is relatively fast and provides helpful ancillary products, including the sun-view geometry, the time of observation, the top-of-atmosphere brightness temperatures in channels 3, 4 and 5, and a cloud mask. Limited quality assurance data accompanies the product. We evaluated the product at one grid cell (8×8 km) over a savanna field site near Skukuza, South Africa. Independent LST estimates derived from field-base endmember measurements suggest the AVHRR product *over that site* has an uncertainty below 1.5 K for daytime retrievals and below 2.5 K for nighttime retrievals. The product accurately tracked warming and cooling trends in surface temperature. Still, a more robust validation program is required before more substantive error estimates can be stated.

The data set developed through this article appears to be satisfactory for large scale analysis of LST trends in time and space. Indeed, it has already been used to reveal LST variability with vegetation structure under different sun-view geometries. It benefits from reuse of proven processing software and consistent algorithm application. Further, it is the only daily (day and night) LST data set for the 1995–2000 time period over Africa of which we know. The complete data set and a user guide are now available through the ORNL DAAC. Readers are urged to heed the cautions in the Discussion concerning product accuracy.

Acknowledgements

We are grateful to Niall Hanan (Colorado State University) for providing us with the Skukuza pyrgeometer data, to Matt Hansen for guidance in the use of the UMD continuous fields product, and Ed Pak for assistance with the GAPS code. This work was part of the SAFARI 2000 Initiative.

References

Becker, F., & Li, Z. -L. (1990). Towards a local split window method over land surfaces. *International Journal of Remote Sensing*, *11*(3), 369–393.

Becker, F., & Li, Z. -L. (1995). Surface temperature and emissivity at various scales: Definition, measurement and related problems. *Remote Sensing Reviews*, *12*, 225–253.

Brutsaert, W., Hsu, A., & Schmugge, T. J. (1993). Parameterization of surface heat fluxes above forest with satellite thermal sensing and boundary-layer soundings. *Journal of Applied Meteorology*, *32*(5), 909–917.

Caselles, V., & Sobrino, J. A. (1989). Determination of frosts in orange groves from NOAA-9 AVHRR data. *Remote Sensing of Environment*, *29*(2), 135–146, doi:10.1016/0034-4257(89)90022-9.

Cracknell, A. (1997). *The Advanced Very High resolution Radiometer (AVHRR).* Taylor and Francis.

FAO–UNESCO. (1987). *Soils of the World*, Food and Agriculture Organization and United Nations Education and Cultural Organization, Elsevier Science Publishing Co. Inc., New York, NY.

Giglio, L., & Justice, C. O. (2003). Effect of wavelength selection on characterization of fire size and temperature. *International Journal of Remote Sensing*, *24*(17), 3515–3520.

Gutman, G. G. (1999). On the monitoring of land surface temperature with the NOAA/AVHRR: Removing the effect of satellite orbit drift. *International Journal of Remote Sensing*, *20*(17), 3407–3413.

Gutman, G., Tarpley, D., Ignatov, A., & Olson, S. (1995). The enhanced NOAA Global Land Dataset from the Advanced Very High Resolution Radiometer. *Bulletin of the American Meteorological Society*, *76*(7), 1141–1156.

Hansen, M. C., DeFries, R. S., Townshend, J. R. G., & Sohlberg, R. (2000). Global land cover classification at 1 km spatial resolution using a classification tree approach. *International Journal of Remote Sensing*, *21* (6–7), 1331–1364.

Holben, B. N., Eck, T. F., Slutsker, I., Tanre, D., Buis, J. P., Setzer, A., et al. (1998). AERONET — A federated instrument network and data archive for aerosol characterization. *Remote Sensing Environment*, *66*, 1–16.

ITT (1994). *AVHRR/2 alignment and calibration handbook (SN204).* Indiana: Fort Wayne.

Jin, M. (2004). Analysis of Land Skin Temperature using AVHRR Observations. *Bulletin of the American Meteorological Society*, *85*(4), 587–600.

Jin, M. L., & Treadon, R. E. (2003). Correcting the orbit drift effect on AVHRR land surface skin temperature measurements. *International Journal of Remote Sensing*, *24*(22), 4543–4558.

Kerr, Y. H., Guillou, C., Lagouarde, J. P., Nerry, F., & Ottlé, C. (1998). *World land surface temperature atlas 1992–1993: LST processor: Algorithm theoretical basis document.* European Space Agency.

Kidwell, K. (1991), *NOAA polar orbiter data* (*TIROS-N*, *NOAA-6*, *NOAA-7*, *NOAA-9*, *NOAA-10*, *NOAA-11 and NOAA-12*) *user's guide*. National Oceanic and Atmosphere Administration, National Environmental Satellite, Data, and Information Service, Washington DC.

Kidwell, K. (1995), *Polar Orbiter Data User's Guide*. U.S. Department of Comerce, NOAA/National Environmental Satellite Data and Information Service, National Climate Data Center, Satellite Data Services Division. 126 pp.

Kustas, W. P., & Norman, J. M. (1996). Use of remote sensing for evapotranspiration monitoring over land surfaces. *Hydrological Sciences*, *41*(4), 495–515.

Moran, M. S., & Jackson, R. D. (1991). Assessing the spatial-distribution of evapotranspiration using remotely sensed inputs. *Journal of Environmental Quality*, *20*(4), 725–737.

Morisette, J. T., Privette, J. L., & Justice, C. O. (2002). A framework for the validation of MODIS Land products. *Remote Sensing of Environment*, *83* (1–2), 77–96.

Myneni, R. B., Keeling, C. D., Tucker, C. J., Asrar, G., & Nemani, R. R. (1997). Increased plant growth in the northern high latitudes from 1981 to 1991. *Nature*, *386*(6626), 698–702.

Nemani, R. R., Keeling, C. D., Hashimoto, H., Jolly, W. M., Piper, S. C., Tucker, C. J., et al. (2003). Climate-driven increases in global terrestrial net primary production from 1982 to 1999. *Science*, *300*(5625), 1560–1563.

Norman, J. M., & Becker, F. (1995). Terminology in thermal infrared remote sensing of natural surfaces. *Remote Sensing Reviews*, *12*, 159–173.

Pinheiro, A. C. T., Privette, J. L., & Guillevic, P. (2006). Modeling the Observed Angular Anisotropy of Land Surface Temperature in a Savanna. *IEEE Transactions on Geosciences Remote Sensing*, *44*(4), 1036–1047.

Pinheiro, A. C. T., Privette, J. L., Mahoney, R., & Tucker, C. J. (2004). Directional effects in a daily AVHRR land surface temperature dataset over Africa. *IEEE Transactions on Geosciences Remote Sensing*, *42*(9), 1941–1954.

Prata, A. J. (1994). Land surface temperature derived from the advanced very high resolution radiometer and the along-track scanning radiometer: 2. Experimental results and validation of AVHRR algorithms. *Journal of Geophysical Research*, *99*(D6), 13025–13058.

Prata, A. J. (2000). *Global distribution of maximum land surface temperature inferred from satellites: Implications for the operation of the advanced along track scanning radiometer.CSIRO atmospheric research technical paper*, *vol. 46*. ISBN 0 643 06503 2. Aspendale, Victoria, Australia.

Price, J. C. (1991). Timing of NOAA afternoon passes. *International Journal of Remote Sensing*, *12*(1), 193–198.

Privette, J. L., Fowler, C., Wick, G. A., Baldwin, D., & Emery, W. J. (1995). Effects of orbital drift on advanced very high resolution radiometer products: Normalized difference vegetation index and sea surface temperature. *Remote Sensing of Environment*, *53*(3), 164–171.

Rosborough, G. W., Baldwin, D. G., & Emery, W. J. (1994). Precise AVHRR image navigation. *IEEE Transactions in Geosciences and Remote Sensing*, *32*(3), 644–657.

Scholes, R. J., Gureja, N., Giannecchinni, M., Dovie, D., Wilson, B., Davidson, N., et al. (2001). The environment and vegetation of the flux measurement site near Skukuza, Kruger National Park. *Koedoe*, *44*(1), 73–83.

Sellers, P. J., Hall, F. G., Asrar, G., Strebel, D. E., & Murphy, R. E. (1988). The first ISLSCP field experiment (FIFE). *Bulletin of the American Meteorological Society*, *69*(1), 22–27.

Sobrino, J. A., Raissouni, N., & Li, Z. -L. (2001). A comparative study of land surface emissivity retrieval from NOAA data. *Remote Sensing Environment*, *75*, 256–266.

Stowe, L. L., Davis, P. A., & McClain, E. P. (1999). Scientific basis and initial evaluation of the CLAVR-1 global clear/cloud classification algorithm for the Advanced Very High Resolution Radiometer. *Journal of Atmospheric and Oceanic Technology*, *16*, 656–681.

Tucker, C. J., Newcomb, W. E., & Dregne, H. E. (1994). Improved data sets for determination of desert spatial extent. *International Journal of Remote Sensing*, *15*, 3519–3545.

Tucker, C. J., Slayback, D. A., Pinzon, J. E., Los, S. O., Myneni, R. B., & Taylor, M. G. (2001). Higher Northern latitude normalized difference vegetation index and growing season trends from 1982 to 1999. *International Journal of Biometeorology*, *45*(4), 184–1990.

Ulivieri, C., Castronuovo, M. M., Francioni, R., & Cardillo, A. (1994). A split window algorithm for estimating land surface temperature from satellites. *Advances in Space Research*, *14*(3), 59–65.

Van de Griend, A. A., & Owe, M. (1993). On the relationship between thermal emissivity and the normalized difference vegetation index. *International Journal of Remote Sensing*, *14*(6), 1119–1131.

Vazquez, D. P., Reyes, F. J. O., & Arboledas, L. A. (1997). A comparative study of algorithms for estimation of land surface temperature from AVHRR. *Remote Sensing Environment*, *62*, 215–222.

Wan, Z., Zhang, Y., QZhang, Q., & Li, Z. -L. (2002). Validation of the land-surface temperature products retrieved from Terra Moderate Resolution Imaging Spectroradiometer data. *Remote Sensing Environment*, *83*, 163–180.

Weinreb, M. P., Hamilton, G., Brown, S., & Koczor, R. (1990). Nonlinearity corrections in calibration of advanced very high resolution radiometer infrared channels. *Journal of Geophysical Research*, *95*(C5), 7381–7388.

Wilber, A. C., Kratz, D. P., & Gupta, S. K. (1999). *Surface emissivity maps for use in satellite retrievals of longwave radiation, NASA/TP-1999-209362.* Hampton, VA: Langley Research Center.

Yu, Y., Privette, J.L., Pinheiro, A.C. and Vogel, R. (submitted for publication), Theoretical evaluation of split window methods to retrieve land surface temperature, *IEEE Trans. Geosci. Remote Sensing*.